

Dynamics of simultaneously measured non-commuting observables

Shay Hacoheh-Gourgy^{†,1,2,*}, Leigh S. Martin^{†,1,2,3,†}, Emmanuel Flurin^{1,2,}

Vinay V. Ramasesh^{1,2}, K. Birgitta Whaley^{3,4}, and Irfan Siddiqi^{1,2}

¹*Quantum Nanoelectronics Laboratory, Department of Physics,
University of California, Berkeley CA 94720, USA.*

²*Center for Quantum Coherent Science, University of California, Berkeley CA 94720, USA.*

³*Berkeley Center for Quantum Information and Computation, Berkeley, California 94720, USA. and*

⁴*Department of Chemistry, University of California, Berkeley, California 94720, USA.*

(Dated: July 6, 2022)

In quantum mechanics, measurement restores a classical notion of reality via collapse of the wavefunction, which yields a precisely defined outcome. On the other hand, the Heisenberg uncertainty principle dictates that incompatible observables, such as position and momentum, cannot both take on arbitrarily precise values. But how does a wavefunction evolve when two such quantities are probed simultaneously, and how does the uncertainty principle dynamically inhibit precise measurement outcomes? To realize this unexplored regime[1–3], we simultaneously apply two continuous quantum non-demolition probes of non-commuting observables on a superconducting qubit. We achieve this capability by developing a novel measurement scheme that allows us to control the axes of multiple readout channels. We show that the uncertainty principle directly governs the dynamics of the state, and consequently standard wavefunction collapse is replaced by a persistent diffusion that exhibits several distinct regimes. Although evolution of the state now differs drastically from that of a conventional measurement, information about both non-commuting observables is extracted by keeping track of the time ordering of the measurement record, enabling quantum state tomography without alternating measurements. Our work creates new capabilities for quantum control, including rapid state purification[4], adaptive measurement[5, 6], measurement-based state steering and continuous quantum error correction[7]. As physical quantum systems interact with their environments via non-commuting degrees of freedom, our work offers a new, more natural approach to experimentally study contemporary quantum foundations[8–13].

Fundamentally non-classical aspects of quantum theory arise from the fact that conjugate properties of a system, such as position and momentum, are incompatible. The celebrated Heisenberg uncertainty principle asserts that such quantities cannot have simultaneously well-defined values in any possible quantum state. As a consequence, simultaneous projective measurements of incompatible observables, along with the accompanying instantaneous wavefunction collapse, are also prohibited. However, such infinitely strong measurements are an idealization. Real measurements acquire information over a finite duration, and wavefunction collapse is in practice a continuous process. In contrast to projective measurements, the uncertainty principle does not preclude simultaneous weak measurement of incompatible properties[3], but rather imposes constraints on the behavior of the system. Here we implement a quantum non-demolition readout of the angular momentum about two different axes of an artificial spin-1/2 system, and observe in real-time the resulting dynamics. Importantly, our measurements are designed to be individually quantum non-demolition, which ensures that the back-action arises only from the competition between incompatible observables.

Our experiment utilizes a single superconducting transmon qubit coupled dispersively to a multimode waveguide cavity[14]. This results in a qubit-state dependent shift of the cavity mode frequency. By prob-

ing a single cavity mode, one can realize a measurement of the qubit state[15]; this readout scheme has been used extensively with superconducting qubits for quantum information processing, and also to perform weak measurements[16] and track quantum trajectories of a single qubit[17]. In our configuration, each cavity mode constitutes a measurement channel which extracts the projection of the qubit spin along the σ_z axis of the Bloch sphere.

The key ingredient to measuring non-commuting observables is to re-engineer the underlying Hamiltonian so that each cavity mode couples to a controllable axis of the qubit. We accomplish this with what we call a single quadrature measurement (SQM), motivated by the back-action evading techniques recently conceived for optomechanical systems[18, 19]. The central idea is to drive Rabi oscillations $\Omega_R/2\pi = 40$ MHz on the qubit so that it Raman scatters a pair of applied sideband tones to the cavity frequency. Interference between the up- and down-converted photons is determined by the relative phase of the sidebands, and dictates which qubit observable is encoded in the resulting signal. The experimental setup is depicted in Fig. 1a. As illustrated in Fig. 1b, the dynamics are governed by a coherent sum of two effective Hamiltonians, a cavity-mediated cooling induced by the lower sideband and a heating due to the upper sideband[20],

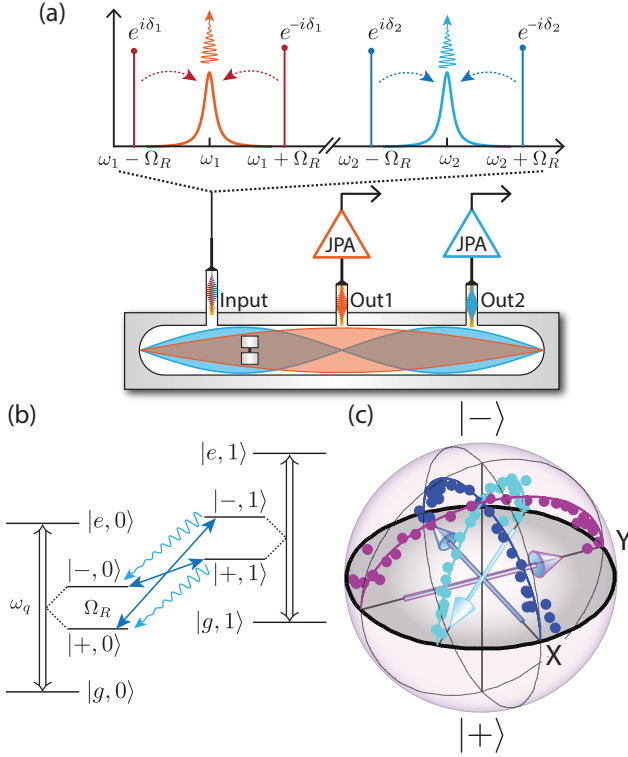


FIG. 1: **Multimode single quadrature measurement (SQM)** (a) A transmon qubit in an aluminum cavity. Via the input port, we drive Rabi oscillations at frequency Ω_R and apply $\pm\Omega_R$ sideband tones to each of the two lowest cavity modes. Each output is monitored using a lumped-element Josephson parametric amplifier (LJPA)[31]. Coupling is designed so that $\sim 90\%$ of each signal is routed to its corresponding LJPA. This system yields two separate measurement channels, each with a controllable measurement basis. (b) Dressed state picture of the SQM scheme for one of the cavity modes. Sideband tones drive transitions indicated by the solid lines, and undulating lines represent cavity decay, which we detect. (c) Tomographic reconstruction after a $1 \mu\text{s}$ SQM applied only to the lower mode, showing collapse along three separately chosen measurement axes σ_{δ_1} , $\delta_1 = \{0, \pi/4, \pi/2\}$. Circles plot tomographic data and lines give theory based on a dephasing rate of $\Gamma_1/2\pi = 122 \text{ kHz}$ and quantum efficiency of $\eta_1 = 0.41$.

$$\begin{aligned}
 H_{\text{eff}} &= \frac{\chi \bar{a}_0}{2} \left[\underbrace{a\sigma^\dagger e^{i\delta} + a^\dagger \sigma e^{-i\delta}}_{\text{resonant heating}} + \underbrace{a\sigma e^{-i\delta} + a^\dagger \sigma^\dagger e^{i\delta}}_{\text{resonant cooling}} \right] \\
 &= \frac{\chi \bar{a}_0}{2} (a + a^\dagger) \sigma_\delta
 \end{aligned} \quad (1)$$

where χ is the qubit-cavity coupling, \bar{a}_0 is the sideband amplitude, a, a^\dagger are the cavity ladder operators and σ, σ^\dagger are the raising and lowering operators with respect to the dressed basis $|\pm\rangle = (|g\rangle \pm |e\rangle)/\sqrt{2}$. Note that this scheme implements longitudinal coupling, an important feature for squeezing-enhanced readout[21]. Importantly,

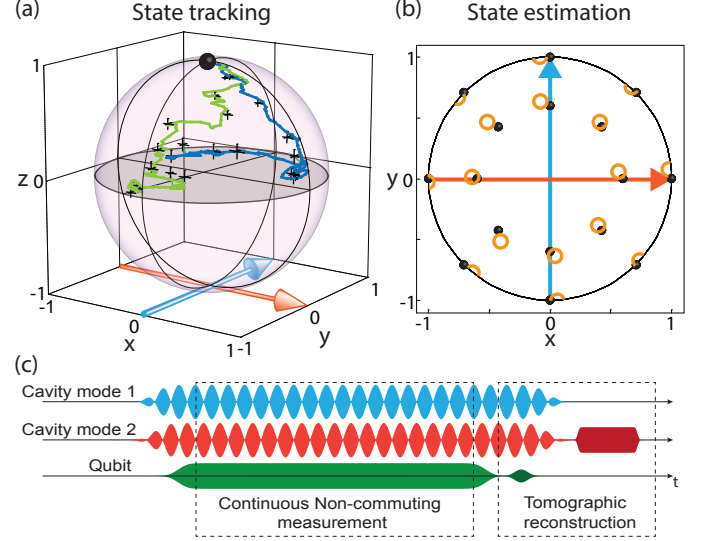


FIG. 2: **Validation of simultaneous non-commuting measurements** (a) Reconstruction of two quantum trajectories initialized at state $|-\rangle$ (black sphere) and their associated tomographic validation. Arrows indicate axis of each measurement. Tomography points are taken every 200 ns, and are linked to the corresponding trajectory time point with a green line. All trajectories ending within ± 0.11 around a given point along the plotted trajectory are used for the corresponding tomography reconstruction. Error bars are generated from statistical uncertainty arising in qubit readout. (b) Estimation of 16 initially unknown state preparations (black spheres) using non-commuting measurements. Orange circles mark 95% confidence intervals, generated by applying maximum likelihood estimation to $\sim 10,000$ trajectories each. (c) Pulse sequence, showing cavity sideband tones and Rabi drive. Tomographic reconstruction consists of a tomography qubit pulse and projective readout.

tantly, the relative sideband phase δ sets the coupling axis $\sigma_\delta \equiv \sigma_x \cos \delta + \sigma_y \sin \delta$. The resulting Hamiltonian is a resonant cavity drive, the sign of which depends on the qubit state along the σ_δ axis. Detecting the cavity output field with quantum efficiency η yields a measurement of the qubit at a rate $\Gamma\eta = 2\chi^2 \bar{a}_0^2 \eta / \kappa$ in the σ_δ basis[15, 22], which we can now control.

First, to demonstrate control of the measurement axis, we perform a single SQM using the lower cavity mode. We prepare the $|-\rangle$ state and read out for $1 \mu\text{s}$ followed by a tomography rotation and a projective measurement using a standard dispersive readout of σ_z . During the SQM, drift in the Rabi frequency and spurious tones at the cavity frequency induce unwanted rotations about the σ_z and σ_δ axes respectively[22]. To mitigate these effects, we actively feedback to stabilize the Rabi frequency to within 10 kHz and suppress leakage of the local oscillator used to generate the sidebands to the 10^{-4} photon level. Because a single SQM commutes with itself at all times, the integral of the signal fully specifies the amount of projection onto an eigenstate[17]. We perform

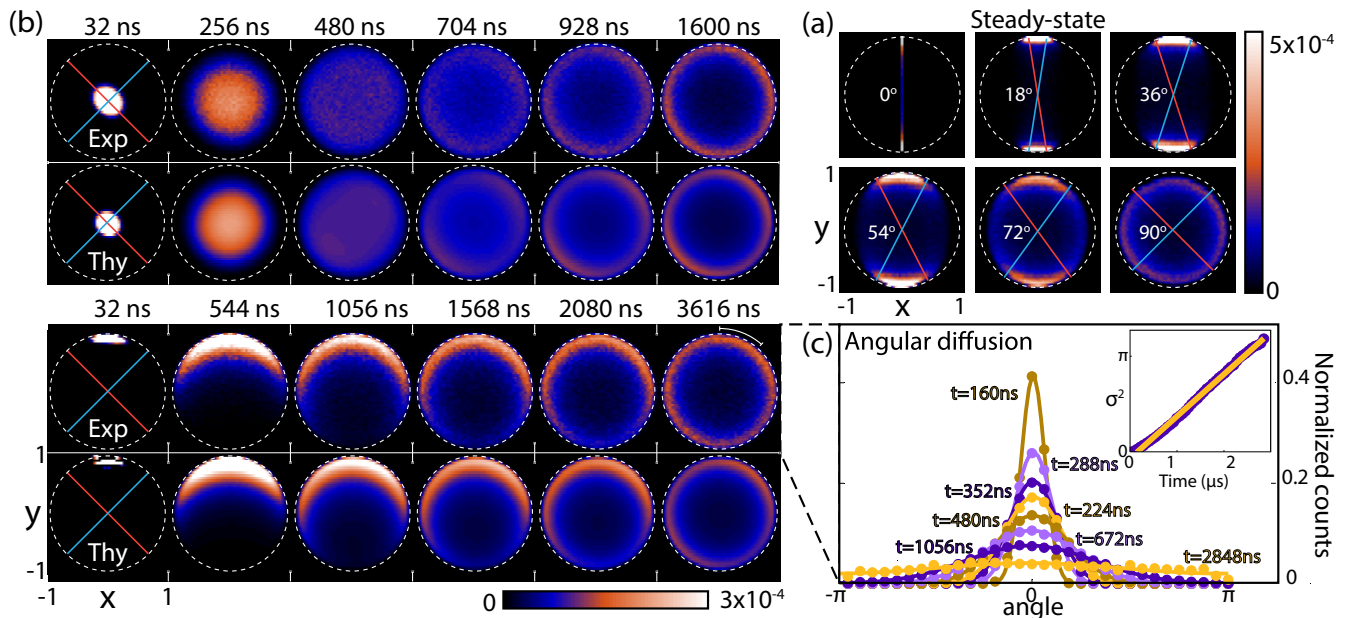


FIG. 3: **Probability distribution of the density matrix** (a) in the steady-state as function of angle, between the axes, demonstrating loss of collapse for non-commuting observables. (b) as function of time for perpendicular measurement axes. We prepare a mixed state for observing the radial dynamics (top), and a state with purity of $P = 0.89$ for observing the azimuthal dynamics (bottom). Upper row of each is experimental data, and bottom row is theoretical comparison derived from the Fokker-Planck equation[22]. (c) Angular probability distributions for states within a ring of inner radius 0.86 and outer radius 0.92, showing that dynamics match those of a random walk. Points are normalized counts and lines are fits to normal distributions convolved with a 2π periodic Dirac comb. Inset – variance as a function of time (violet) and linear fit (yellow) yielding a slope of $1.4 \mu\text{s}^{-1}$. The expected slope for a perfect random walk in our system is $1.5 \mu\text{s}^{-1}$ with the main source of uncertainty due to measurement rate uncertainty of about 10%.

tomographic state validation on subsets of the data post-selected according to this integrated signal. Tomography data in Fig. 1c show state collapse along the desired axis, confirming control of the measurement operator σ_δ .

Next, to simultaneously measure two non-commuting observables, we apply the SQM to the two lowest cavity modes. Each pair of sidebands sets a measurement axis, and thus we are able to control them independently. Because non-commutativity leads to dependence on the time ordering of measurement outcomes, the integral of the output signal is no longer sufficient to uniquely determine the qubit state in general. Nevertheless, the combined measurement records encode complete information, and we are able to track quantum trajectories of an initially known state. We calculate the trajectories by iteratively applying a measurement operator which corresponds to the record of both σ_{δ_1} and σ_{δ_2} integrated over a short interval $\Delta t = 16 \text{ ns}$ [22]. To experimentally verify the trajectories, we perform quantum state tomography[23] on subsets of trajectories that end at approximately the same point on the Bloch sphere. Figure 2a shows two such traces with their tomographic validation from data in which the measurement axes are set to be orthogonal, $\sigma_{\delta_1} = \sigma_x$ and $\sigma_{\delta_2} = \sigma_y$.

Due to the disturbances introduced by measurement

incompatibility, extraction of an initially unknown quantity, such as a Hamiltonian parameter or system observable, requires use of the *combined* measurement records and their full time orderings. In particular, estimation methods must rely not only on the statistics of the measurement records, but also on some estimate of this disturbance. We encode this information in a set of composite measurement operators, one for each each trajectory[22, 24], and use them to reconstruct a set of initial state preparations, analogous to state tomography. We then perform maximum likelihood estimation of the initial state over a large set of trajectories taken with the same initial state[24]. Figure 2b shows reconstruction of sixteen state preparations again in the case of orthogonal measurement axes. Agreement within the confidence interval demonstrates that despite the complicated dynamics induced by competing observables, our scheme performs as a measurement, and that it extracts information about σ_x and σ_y simultaneously.

A state undergoing a non-commuting measurement exhibits dynamics beyond those of usual wavefunction collapse. We directly observe this evolution by measuring the probability distributions of the resulting density matrices. Figure 3a shows the steady state probability distributions. When the axes align, the system collapses to

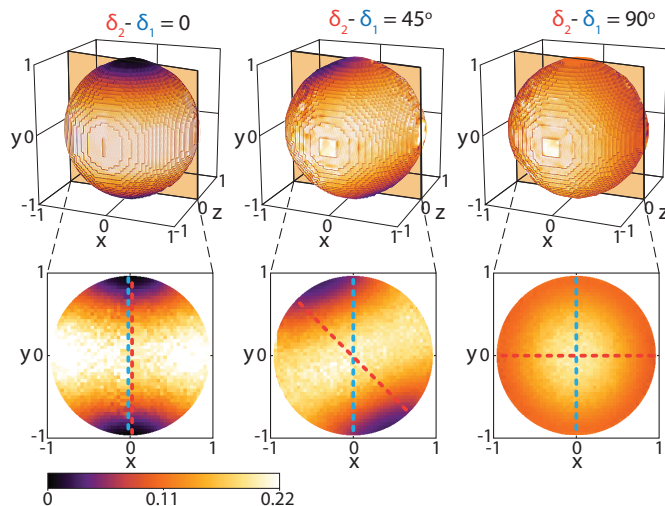


FIG. 4: **Magnitude of the quantum back-action.** The amplitude of disturbance induced by measurement ($\text{Tr}[d\rho^\dagger d\rho]$) at each point on the Bloch sphere for three relative measurement angles $\delta_2 - \delta_1$. (top) Disturbance at the surface of the Bloch sphere, which is bounded from below by the uncertainty principle. (bottom) A slice through the $z = 0$ plane. Dotted lines mark measurement axes. For non-commuting observables ($\delta_2 - \delta_1 \neq 0$), no point of zero disturbance exists within the entire volume of the Bloch sphere, indicating that the state must diffuse indefinitely.

two points at the poles of the Bloch sphere as expected for commuting measurement operators. When the axes are separated by a finite angle less than 90 degrees, the state does not collapse to any point, but rather localizes to regions of finite size defined by the measurement axes. A salient feature is that when the axes are orthogonal and hence maximally incompatible, the location of the measurement axes no longer leaves any imprint on the state evolution. The distinct regions merge and we lose all notion of collapse.

Figure 3b shows probability distributions as a function of time for this canonical case. Starting in a mixed state, we see that the state purifies isotropically to a mean steady-state radius given by $r = \sqrt{\eta}$. High quantum efficiency in our system allows us to observe the azimuthal dynamics by preparing a state of purity $P = 0.89$, the most likely steady-state purity. As predicted by [2] in the case of unit quantum efficiency, competition between the maximally incompatible observables leads to diffusive motion given by a uniform random walk. Figure 3c shows the angular distribution as a function of time, which agrees quantitatively with this prediction.

The diffusive behavior seen in Fig. 3c suggests that even once the probability distributions have reached steady state, the system continues to evolve. To quantify this measurement-induced disturbance, we plot the norm of the state change $d\rho$ over an interval of 64 ns versus position on the Bloch sphere in Fig. 4. When the measure-

ments are compatible, two points on the Bloch sphere exhibit zero disturbance, which indicate mutual eigenstates of the measurements and hence points of collapse. No such points exist when the measurements are incompatible, implying that the state diffuses indefinitely. If we calculate this disturbance directly from the stochastic master equation for the system, we find the following relation valid for all initially pure states

$$\begin{aligned} \text{Tr}[d\rho^\dagger d\rho] &= (\Delta\sigma_{\delta_1}^2\Gamma_1\eta_1 + \Delta\sigma_{\delta_2}^2\Gamma_2\eta_2)dt \\ &\geq |[\sigma_{\delta_1}, \sigma_{\delta_2}]| \sqrt{\eta_1\eta_2\Gamma_1\Gamma_2}dt \end{aligned} \quad (2)$$

which holds for any Hermitian operators of any system. The right hand side of the equality closely resembles the original Heisenberg uncertainty relation, but contains the sum of the variances instead of the product. Unlike the latter, the sum can be bounded by a stronger inequality which is never trivial for non-commuting measurements[25]. This shows that the persistent diffusion observed in Fig. 3c is a universal consequence of the uncertainty principle and can be quantitatively derived from it.

The techniques we developed readily generalize to multi-level and multi-qubit systems, and have numerous potential applications for quantum information science. The ability to measure multiple distinct operators of a quantum system simultaneously could allow for implementation of continuous quantum error correction, in which several error syndromes can be monitored concurrently[7]. By monitoring a third mode and applying an additional drive, the axis perpendicular to the Rabi plane can also be probed[26]. With a modest improvement in quantum efficiency, our scheme will also lead to faster initialization of quantum circuits[4, 27].

Our experiment reveals the subtle interplay between the Heisenberg uncertainty principle and wavefunction collapse. Since incompatibility of observables is at the core of quantum theory[28], the ability to continuously measure non-commuting observables offers new ways to investigate essential features of quantum mechanics such as contextuality[8, 9] and error-disturbance bounds[10–13]. Thus our work provides an indispensable tool for investigating this virtually unexplored territory of quantum foundations.

METHODS

Experimental setup and sample. Our transmon qubit is fabricated on double-side-polished silicon, with a single double-angle-evaporated Al/AlO_x/Al Josephson junction. The internal dimensions of the aluminum 3D cavity are 81 mm x 51 mm x 20 mm. The qubit is positioned 23 mm from the edge of the cavity. The qubit is characterized by a charging energy $E_c/h = 220$ MHz and a $|0\rangle$ to $|1\rangle$ transition frequency $\omega_q/h = 4.262$ GHz. The qubit coherence is characterized by an excited state lifetime of $T_1 = 60$ μ s, echo time of $T_{2,\text{echo}} = 40$ μ s and Rabi decay time of 25 μ s. The two lowest cavity modes used in the experiment have frequencies $\omega_1/2\pi = 6.666$ GHz, $\omega_2/2\pi = 7.391$ GHz, linewidths $\kappa_1/2\pi = 7.2$ MHz, $\kappa_2/2\pi = 4.3$ MHz and qubit dispersive frequency shift $\chi_1/2\pi = 0.18$ MHz, $\chi_2/2\pi = 0.23$ MHz respectively. The cavity outputs are amplified using two lumped-element Josephson parametric amplifiers (LJPA) operated in phase sensitive mode. Amplifier gains are set to 15 dB for mode 1 and 18 dB for mode 2. To prevent saturation of the amplifiers by the SQM sideband tones, we designed them to have relatively narrow bandwidths of 20 MHz bandwidth for mode 1 with 7.3 MHz bandwidth for mode 2. The signals are further amplified with two cryogenic HEMT amplifiers, model number LNF4.8. Due to a high noise temperature of HEMT 1, we added a Josephson traveling wave parametric amplifier[29] immediately before it.

In order to route signal from mode i only to the corresponding LJPA, the pin coupling to mode 1 is placed at the node of mode 2 (see Fig. 1), so that photons from mode 2 do not couple to it. Placement of pin 2 and the choice of $\kappa_1 > \kappa_2$ reduces leakage of mode 1 signal into pin 2. A small amount of signal from modes 1 and 2 is also lost through the input pin. We estimate the total reduction in quantum efficiency due to these loss channels to be approximately 10% for each mode. The total quantum efficiencies are $\eta_1 = 0.41$ and $\eta_2 = 0.49$ for modes 1 and 2 respectively.

Measurement Calibration. We generate SQM sideband tones by mixing a common local oscillator (LO) set to the corresponding cavity frequency with 40 MHz tones and controllable DC offsets input to the I and Q ports of a mixer. The output is followed by an amplifier model ZRON8G+ and then passed through a home built notch filter which attenuates the carrier by ~ 25 dB relative to the sideband tones. The filter and DC offset controls allow suppression of the LO to the 10^{-4} photon number level, which eliminates spurious rotations about the measurement axis. We balance the relative amplitudes of the sideband tones by measuring the induced cooling or heating with Ramsey interferometry[20], and then adjusting the relative phase between the I and Q 40 MHz signals.

Since the sideband tones stark shift the qubit, all qubit

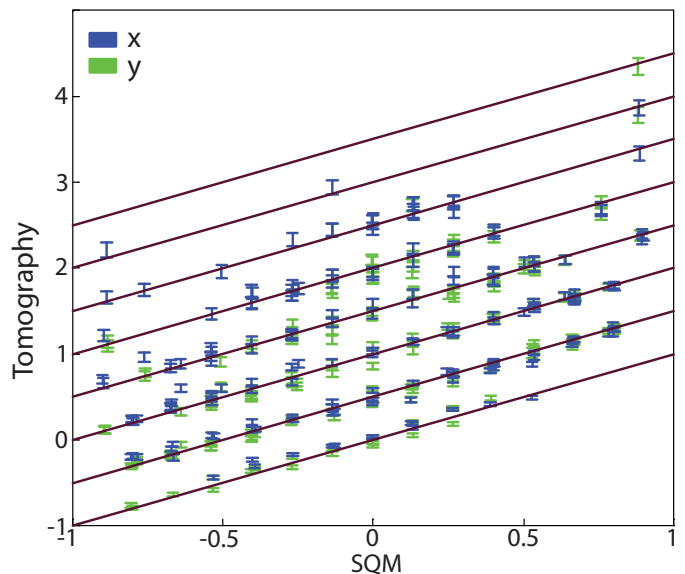


FIG. 5: SQM vs tomographic validation Tomographic validation of a set of trajectories initialized in the state $y = -1$ and tracked for 3μ s, with the axes being perpendicular. Horizontal axis indicates Bloch sphere coordinate as predicted by trajectory reconstruction. Vertical axis represents the coordinate reconstructed from post-selected tomography data. Error bars are derived from the Poisson statistics of the qubit measurement. Data are staggered vertically to allow for clearer visualization by adding one of seven arbitrary offsets. These offsets are chosen according to the number of measurements contributing to each data point.

drives and pulses are applied with the sidebands present and at the Stark-shifted qubit frequency, so that the experiment takes place entirely in this frame. The Rabi frequency is chosen such that the measurement operates in the unresolved sideband regime $\Omega_R \gg \kappa$. The sideband tone powers are set such that the measurement rate is much slower than the cavity mode bandwidths, so that the polaron transformation[15] holds when both measurements are on.

After setting up the SQM sidebands, one must carefully set the Rabi frequency to 40 MHz. Furthermore, because the Rabi frequency ramps up over a finite duration, the relative phase between the lab frame and Rabi frame is also unknown and must be measured. We jointly calibrated these parameters by sweeping both the SQM axis and the Rabi frequency. Extended data Fig. 6 shows the integrated SQM signal over 7 μ s as a function of these two sweep parameters. When the initial qubit state is aligned with the measurement axis and the Rabi frequency is 40.00 MHz, the output signal is maximal. Alignment between the initial qubit state and the measurement axis indicates that the phase between the lab and Rabi frames is now known. Rotation of the qubit during the measurement leads to the slight tilt evident in extended data Fig. 6, which means that a 1D sweep

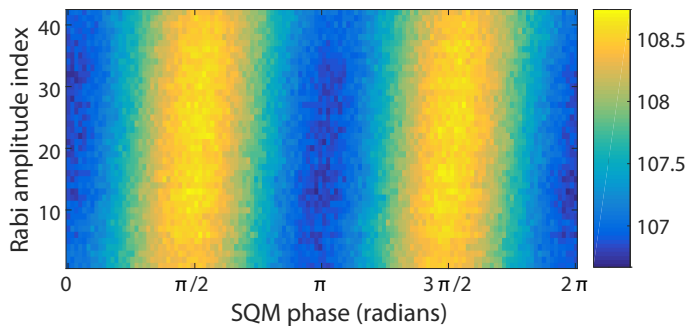


FIG. 6: **SQM calibration** Integrated SQM signal for measurement calibration given in digitizer units (0-255). Vertical sweep is performed by sweeping the modulation amplitude to drive approximately 40 MHz Rabi oscillations.

of just the phase or Rabi amplitude would be insufficient to accurately find the global maximum.

Temperature drifts in the room-temperature electronics lead to instability of the Rabi frequency, which induces dephasing along the σ_z axis of the qubit in the measurement frame. To efficiently and precisely measure this drift, we perform a $1 \mu s$ SQM followed by a lab-frame readout of σ_z . This duration is chosen so that $\langle \sigma_z \rangle \approx 0$, which means that the readout is maximally sensitive to drift in the Rabi frequency. We use this signal to stabilize the Rabi frequency by applying feedback every few seconds while taking trajectory data.

In order to measure quantum trajectories, we require an accurate estimate of the SQM rates Γ_i and quantum efficiencies η_i . The former we measure by preparing $|+\rangle$ and then making a Ramsey measurement. We measure the quantum efficiency by preparing states aligned and anti-aligned with the SQM. Histograms of the integrated measurement records yield a pair of Gaussians which separate as a function of time. The quantum efficiency is given by[30].

$$\eta_i = \frac{(\mu_\uparrow - \mu_\downarrow)^2}{8\tau\sigma^2\Gamma_{D,i}} \quad (3)$$

where $\mu_{\uparrow/\downarrow}$ is the mean of the Gaussian for the aligned/anti-aligned state preparation, σ is the average standard deviation of the Gaussians and τ is the measurement duration.

In order to validate our system calibration and quantum trajectory reconstructions, we apply one of seven tomography pulses $\{\text{Identity}, \pi/2_x, -\pi/2_x, \pi/2_y, -\pi/2_y, \pi_x, -\pi_x\}$ at the end of each trajectory followed by a dispersive readout in the lab frame. Extended data Fig. 5 shows comparison between tomographic estimates of $\langle \sigma_x \rangle$ and $\langle \sigma_y \rangle$ and their corresponding estimates from trajectory reconstruction. To generate the tomographic validation data, we have partitioned the Bloch sphere into a $15 \times 15 \times 15$

grid for post-selection. Each data point is a tomographic measurement of all trajectories which were predicted to end within the corresponding voxel. 57% of data points lie within error bars, indicating good agreement and low contribution of systematic errors.

Single Quadrature Measurement. Our system is described by the following dispersive Hamiltonian

$$H = H_q + H_{\text{drive}} + \sum_{i=\{1,2\}} (\omega_{c,i} + \chi_i \sigma_z) a_i^\dagger a_i \quad (4)$$

$$H_q = \frac{\omega_q}{2} \sigma_z + \Omega_R (\sigma + \sigma^\dagger) \cos(\omega_d t)$$

$$H_{\text{drive}} = \sum_{i=\{1,2\}} \epsilon_i(t) a_i^\dagger + \epsilon_i(t)^* a_i$$

where $\epsilon_i(t) \in \mathbb{C}$ is the coherent drive that will represent the SQM sideband drives. The master equation for a cavity which is damped at rate κ_i and monitored with quantum efficiency η_i is

$$d\rho = -i[H, \rho]dt + \sum_{i=\{1,2\}} \kappa_i \mathcal{D}[a_i]\rho dt + \sqrt{\kappa_i \eta_i} \mathcal{H}[a_i e^{i\phi_i}] \rho dW_i \quad (5)$$

where $\mathcal{D}[X]\rho = X\rho X^\dagger - (X^\dagger X\rho + \rho X^\dagger X)/2$ is the dissipation superoperator, $\mathcal{H}[X]\rho = X\rho + \rho X^\dagger - \langle X\rho + \rho X^\dagger \rangle \rho$ and ϕ_i is the amplification axis of the phase sensitive amplifier used to monitor mode i . dW_i is a Gaussian distributed variable with variance dt extracted from measurement record i . For the derivation, it suffices to consider just one of the two cavity modes. To measure a single quadrature of the qubit, we drive the cavity with a pair of sidebands detuned by $\pm\Omega_R$ from the cavity resonance, and with phases $\pm(\delta - \text{atan}(\kappa/2\Omega_R))$. As $\Omega_R \gg \kappa$, the latter term can be ignored in our experiment. We choose this drive $\epsilon(t) = -i\bar{a}_0 \sqrt{\Omega_R^2 + \kappa^2/4} \sin(\Omega_R t + \delta - \text{atan}(\kappa/2\Omega_R)) e^{-i\omega_c t}$ so that the cavity internal displacement due to the sidebands takes the form

$$\bar{a}(t) = \bar{a}_0 \cos(\Omega_R t + \delta) e^{-i\omega_c t} \rightarrow \bar{a}_0 \cos(\Omega_R t + \delta). \quad (6)$$

The right arrow indicates that we have transformed into the interaction picture with respect to the cavity. We take \bar{a}_0 to be real for simplicity and define the displaced cavity operator $d = a - \bar{a}$. We first transform the cavity dissipation terms

$$\kappa \mathcal{D}[a]\rho = \kappa \mathcal{D}[d + \bar{a}]\rho = \kappa \mathcal{D}[d]\rho - i[H_{\text{dis}}, \rho] \quad (7)$$

$$H_{\text{dis}} = -\frac{i\kappa}{2} (\bar{a}d^\dagger - \bar{a}^*d)$$

$$\sqrt{\kappa\eta}\mathcal{H}[ae^{i\phi}] = \sqrt{\kappa\eta}\mathcal{H}[de^{i\phi}].$$

This change of variables is equivalent to transforming the Hamiltonian by the displacement operator $\exp(\bar{a}a^\dagger -$

$\bar{a}a$), and thus adds a term $H' = i(\bar{a}d - \dot{\bar{a}}d^\dagger)$ to the Hamiltonian. Note that H_{dis} and H' cancel the drive term H_{drive} from Eq. (4). Writing the remaining terms of H for one cavity mode in the interaction picture with respect to the cavity and in the frame of the qubit drive (*i.e.* transforming the Hamiltonian by $\exp[i\omega_c a^\dagger at + i\omega_d \sigma_z t/2]$) and applying the rotating wave approximation, we find

$$\begin{aligned} H_{\text{int}} &= \chi a^\dagger a \sigma_z + H_{q,\text{int}} \\ &= \chi[(d^\dagger + \bar{a}^*)(d + \bar{a})\sigma_z + H_{q,\text{int}}] \\ &= \chi \left[\bar{a}_0 \cos(\Omega_R t + \delta)(d^\dagger + d) + \frac{\bar{n}_0}{2} \right. \\ &\quad \left. + \bar{n}_0 \frac{\cos(2\Omega_R t + 2\delta)}{2} + d^\dagger d \right] \sigma_z + H_{q,\text{int}} \\ H_{q,\text{int}} &= \frac{1}{2}[(\omega_q - \omega_d)\sigma_z + \Omega_R \sigma_x] \end{aligned} \quad (8)$$

where we have defined $\bar{n}_0 = \bar{a}_0^2$. Choosing the Rabi drive to be resonant (*i.e.* $\omega_q - \omega_d = -\chi\bar{n}_0$), we now go into the Hadamard frame ($\sigma_z \leftrightarrow \sigma_x$), and then go into a frame rotating at the Rabi frequency ($\exp[i\Omega_R \sigma_z t/2]$). These transformations eliminate $H_{q,\text{int}}$ and map σ_z to $\sigma e^{-i\Omega_R t} + \sigma^\dagger e^{i\Omega_R t}$, so the Hamiltonian becomes

$$\begin{aligned} H_{q\text{-frame}} &= \frac{\chi \bar{a}_0}{2} (e^{i\Omega_R t + i\delta} + e^{-i\Omega_R t - i\delta})(d^\dagger + d) \\ &\quad \times (\sigma e^{-i\Omega_R t} + \sigma^\dagger e^{i\Omega_R t}) \\ &\quad + \chi \left[\bar{n}_0 \frac{\cos(2\Omega_R t + 2\delta)}{2} + d^\dagger d \right] (\sigma e^{-i\Omega t} + \sigma^\dagger e^{i\Omega_R t}). \end{aligned} \quad (9)$$

Dropping terms which rotate at Ω_R or $2\Omega_R$, we are left with

$$\begin{aligned} H_{q\text{-frame}} &= \frac{\chi \bar{a}_0}{2} (d^\dagger + d)(\sigma e^{i\delta} + \sigma^\dagger e^{-i\delta}) = \tilde{g} \sigma_\delta (d^\dagger + d) \\ \sigma_\delta &\equiv \cos(\delta)\sigma_x + \sin(\delta)\sigma_y \\ \tilde{g} &\equiv \frac{\chi \bar{a}_0}{2} \end{aligned} \quad (10)$$

which is a qubit-state-dependent cavity drive Hamiltonian.

If in addition to the sideband tones, a small amount of LO leakage (photons at the frequency of the mode) is also present at the cavity input, then Eq. 6 would read $\bar{a}_0 \cos(\Omega_R t + \delta) + \bar{a}_{\text{LO}}$, and the effective Hamiltonian would instead be

$$H_{q\text{-frame}} = \tilde{g} \sigma_\delta (d^\dagger + d + 2\text{Re}[\bar{a}_{\text{LO}}]). \quad (11)$$

Thus LO leakage induces unwanted rotations about the σ_δ axis.

If the cavity starts in the ground state when this Hamiltonian is turned on, then it remains in a coherent state at all times. To derive an effective master equation

for the qubit, we must eliminate the cavity entirely from Eq. (5). This may be accomplished by first applying a transformation which displaces the cavity to its ground state, which is known as the polaron transformation[15]

$$\begin{aligned} U &= |e_\delta\rangle\langle e_\delta| D[\alpha_e] + |g_\delta\rangle\langle g_\delta| D[\alpha_g] \\ \dot{\alpha}_{e/g} &= -i\epsilon_{e/g} - \frac{\kappa}{2}\alpha_{e/g} \quad \epsilon_{e/g} = \pm \tilde{g} \end{aligned} \quad (12)$$

where D is the cavity displacement operator, $|e_\delta/g_\delta\rangle$ are the eigenstates of σ_δ and $\alpha_{e/g}$ is the cavity displacement conditional on the qubit state. Because the second line is the classical equation of motion for a resonantly driven cavity with drive rate ϵ and damping κ , this transformation maps the cavity to its ground state at all times, allowing us to trace it out. Transforming back from the polaron frame to the lab frame, we find that the effective stochastic master equation for the qubit is

$$d\rho = \mathcal{L}\rho dt + \frac{\sqrt{\Gamma_M}}{2} \mathcal{H}[\sigma_\delta]\rho dW - i \frac{\sqrt{\Gamma'_M}}{2} [\sigma_\delta, \rho] dW \quad (13)$$

$$\mathcal{L}\rho = -i \frac{B}{2} [\sigma_\delta, \rho] + \frac{\Gamma}{2} \mathcal{D}[\sigma_\delta]\rho$$

$$B = 2\tilde{g}\text{Re}(\alpha_e + \alpha_g) \quad \Gamma = -2\tilde{g}\text{Im}(\alpha_e - \alpha_g)$$

$$\sqrt{\Gamma_M} = \sqrt{\kappa\eta}|\beta| \cos(\phi - \theta_\beta) \quad \sqrt{\Gamma'_M} = \sqrt{\kappa\eta}|\beta| \sin(\phi - \theta_\beta)$$

$$\beta = \alpha_e - \alpha_g$$

where $\theta_\beta = \arg(\beta)$ is the angle of the cavity displacement axis β in the IQ plane and Γ is the dephasing rate. Substituting the equations of motion for the cavity into the remaining expressions, we find

$$\begin{aligned} d\rho &= \frac{4\tilde{g}^2}{\kappa} (1 - e^{-\kappa t/2}) \mathcal{D}[\sigma_\delta]\rho dt + \\ &\quad \sqrt{\frac{4\tilde{g}^2}{\kappa}} \eta (1 - e^{-\kappa t/2}) \mathcal{H}[e^{i\phi}\sigma_\delta]\rho dW \\ \implies \Gamma &= \frac{8\tilde{g}^2}{\kappa} = \frac{2\chi^2 \bar{n}_0}{\kappa}. \end{aligned} \quad (14)$$

We align the LJPA amplification axis to the axis of displacement arising in Eq. 10, so that $\phi = \theta_\beta$. Application of sidebands to another mode of the cavity does not change the above derivation except to add an additional measurement modeled by Eq. 14. Neglecting time-scales of order $1/\kappa$, measurement of two observables σ_{δ_1} and σ_{δ_2} is modeled by

$$\begin{aligned} d\rho &= \sum_{i=\{1,2\}} \frac{\Gamma_i}{2} \mathcal{D}[\sigma_{\delta_i}]\rho dt + \sqrt{\frac{\Gamma_i \eta_i}{2}} \mathcal{H}[\sigma_{\delta_i}]\rho dW \\ V_i dt &= \langle \sigma_{\delta_i} \rangle dt + \frac{dW_i}{\sqrt{2\eta_i \Gamma_i}} \end{aligned} \quad (15)$$

where V_i is the measurement signal at time t , normalized appropriately. Equation 15 can also be converted to a Fokker Planck equation, which propagates probability distributions of ρ . We use the latter to generate theory plots for Fig. 3. This stochastic master equation is generated by the following measurement operator

$$\Omega(V) = \exp \left[\sum_{i=1,2} -\frac{\Gamma_i \eta_i}{2} (V_i(t) - \sigma_{\delta,i})^2 dt \right] \quad (16)$$

$$\rho(t + dt) = \mathcal{E}_{1-\eta_i} \frac{\Omega \rho(t) \Omega^\dagger}{\text{Tr}[\Omega \rho(t) \Omega^\dagger]}$$

where $\mathcal{E}_{1-\eta_i}$ is a superoperator which models dephasing due to finite quantum efficiency. To assure positivity of the state when dt is taken to be finite, we use Eq. 16 to numerically propagate quantum trajectories and also to calculate probabilities for maximum likelihood reconstruction.

Acknowledgements We thank Justin Dressel, Andrew Jordan, Alexander Korotkov, Joshua Combes, Mohan Sarovar, Uri Vool and Juan Atalaya for invaluable discussions, and MIT Lincoln labs for fabrication of the TWPA. L.S.M. and V.V.R. acknowledge support from the National Science Foundation Graduate Fellowship Grant No. 1106400. L.S.M additionally acknowledges support from the Berkeley Fellowship for Graduate Study. This work was supported by the Air Force Office of Scientific Research under Grant # FA9550-12-1-0378 and the Army Research Office under Grant # W911NF-15-1-0496.

Author Contributions S.H. and L.S.M wrote the manuscript, conducted the experiment and analyzed the data. S.H., L.S.M., E.F. and I.S. conceived of the experiment. S.H. and L.S.M constructed the experimental setup with assistance from V.V.R. and E.F.. S.H. fabricated the qubit and LJPAs. L.S.M. performed theoretical analysis with assistance from S.H. All authors contributed to discussions and preparation of the manuscript. All work was carried out under the supervision of K.B.W. and I.S..

Author Information The authors declare no competing financial interests.

* shayhh@berkeley.edushayhh@berkeley.edu

† These authors contributed equally to this work

- [1] Jordan, A. N. & Büttiker, M. Continuous quantum measurement with independent detector cross correlations. *Phys. Rev. Lett.* **95**, 220401 (2005).
- [2] Ruskov, R., Korotkov, A. N. & Mølmer, K. Qubit state monitoring by measurement of three complementary observables. *Phys. Rev. Lett.* **105**, 1–4 (2010).

- [3] Arthurs, E. & Kelly, J. L. On the Simultaneous Measurement of a Pair of Conjugate Observables. *Bell System Technical Journal* **44**, 725–729 (1965).
- [4] Ruskov, R., Combes, J., Mølmer, K. & Wiseman, H. M. Qubit purification speed-up for three complementary continuous measurements. *Philosophical Transactions of the Royal Society A: Mathematical, Physical and Engineering Sciences* **370**, 5291–5307 (2012).
- [5] Jacobs, K. How to project qubits faster using quantum feedback. *Phys. Rev. A* **67**, 030301 (2003).
- [6] Wiseman, H. M. Adaptive phase measurements of optical modes: Going beyond the marginal q distribution. *Phys. Rev. Lett.* **75**, 4587 (1995).
- [7] Ahn, C., Doherty, A. C. & Landahl, A. J. Continuous quantum error correction via quantum feedback control. *Phys. Rev. A* **65**, 042301 (2002).
- [8] Kirchmair, G. *et al.* State-independent experimental test of quantum contextuality. *Nature* **460**, 494–497 (2009).
- [9] Kochen, S. & Specker, E. P. The Problem of Hidden Variables in Quantum Mechanics. *J Math. Mech.* **17**(1), 59–87 (1968).
- [10] Erhart, J. *et al.* Experimental demonstration of a universally valid error-disturbance uncertainty relation in spin measurements. *Nat. Phys.* **8**, 185–189 (2012).
- [11] Dressel, J. & Nori, F. Certainty in Heisenberg’s uncertainty principle: Revisiting definitions for estimation errors and disturbance. *Phys. Rev. A* **89**, 022106 (2014).
- [12] Nishizawa, A. & Chen, Y. Universally valid error-disturbance relations in continuous measurements. *arXiv preprint arXiv:1506.00304* (2015).
- [13] Ozawa, M. Universally valid reformulation of the Heisenberg uncertainty principle on noise and disturbance in measurement. *Phys. Rev. A* **67**, 042105 (2003).
- [14] Koch, J. *et al.* Charge-insensitive qubit design derived from the Cooper pair box. *Phys. Rev. A* **76**, 042319 (2007).
- [15] Gambetta, J. *et al.* Quantum trajectory approach to circuit QED: Quantum jumps and the Zeno effect. *Phys. Rev. A* **77**, 012112 (2008).
- [16] Hatridge, M. *et al.* Quantum back-action of an individual variable-strength measurement. *Science* **339**, 178–81 (2013).
- [17] Murch, K. W., Weber, S. J., Macklin, C. & Siddiqi, I. Observing single quantum trajectories of a superconducting quantum bit. *Nature* **502**, 211–214 (2013).
- [18] Caves, C. M., Thorne, K. S., Drever, R. W., Sandberg, V. D. & Zimmermann, M. On the measurement of a weak classical force coupled to a quantum-mechanical oscillator. *Rev. Mod. Phys.* **52**, 341 (1980).
- [19] Hertzberg, J. B. *et al.* Back-action-evading measurements of nanomechanical motion. *Nat. Phys.* **6**, 213–217 (2010).
- [20] Murch, K. W. *et al.* Cavity-assisted quantum bath engineering. *Phys. Rev. Lett.* **109**, 1–5 (2012). arXiv:1207.0053.
- [21] Didier, N., Bourassa, J. & Blais, A. Fast quantum non-demolition readout by parametric modulation of longitudinal qubit-oscillator interaction. *Phys. Rev. Lett.* **115**, 203601 (2015).
- [22] Hacohe-Gourgy, S. H. *et al.* Supplementary Methods (2016).
- [23] Nielson, M. A. & Chuang, I. L. *Quantum computation and quantum information* (Cambridge University Press, 2010).

- [24] Six, P. *et al.* Quantum state tomography with noninstantaneous measurements, imperfections, and decoherence. *Phys. Rev. A* **93**, 012109 (2016).
- [25] MacCone, L. & Pati, A. K. Stronger uncertainty relations for all incompatible observables. *Phys. Rev. Lett.* **113**, 1–5 (2014). arXiv:1407.0338.
- [26] Vool, U. *et al.* Continuous quantum nondemolition measurement of the transverse component of a qubit. *arXiv:1605.08004* (2011). arXiv:1605.08004.
- [27] Combes, J., Wiseman, H. M. & Scott, A. J. Replacing quantum feedback with open-loop control and quantum filtering. *Phys. Rev. A* **81**, 020301 (2010).
- [28] Dressel, J. Indirect Observable Measurement: an Algebraic Approach, PhD Thesis, Univ of Rochester (P52) (2013).
- [29] Macklin, C. *et al.* A near quantum-limited Josephson traveling-wave parametric amplifier. *Science* **350**, 307 (2015).
- [30] Korotkov, A. N. Quantum Bayesian approach to circuit QED measurement. *arXiv:1111.4016* 11 (2011). arXiv:1111.4016.
- [31] Castellanos-Beltran, M. A., Irwin, K. D., Hilton, G. C., Vale, L. R. & Lehnert, K. W. Amplification and squeezing of quantum noise with a tunable Josephson metamaterial. *Nat. Phys.* **4**, 929931 (2008).